Study of type-III intermittency in the Landau-Lifshitz-Gilbert equation

J. Bragard[1], J. A. Vélez[2], J. A. Riquelme[3], L. M. Pérez[2], R. Hernández-García[4,5], R. J. Barrientos[4,6], and D. Laroze[2,*]

[1] Departamento de Física y Matemáticas Aplicadas, Universidad de Navarra, Pamplona 31080, Spain.
[2] Instituto de Alta Investigación, CEDENNA, Universidad de Tarapacá, Casilla 7 D, Arica, Chile.
[3] Instituto de Alta Investigación, Sede Esmeralda, Universidad de Tarapacá, Av. Luis Emilio Recabarren 2477, Iquique, Chile.
[4] Laboratory of Technological Research in Pattern Recognition (LITRP), Universidad Católica del Maule, 3480112 Talca, Chile.
[5] Research Center for Advanced Studies of Maule (CIEAM), Universidad Católica del Maule, 3480112 Talca, Chile.
[6] DCI Department, Faculty of Engineering Sciences, Universidad Católica del Maule, 3480112 Talca, Chile.

E-mail: *dlarozen@uta.cl

Abstract. We have studied a route of chaos in the dissipative Landau-Lifshitz-Gilbert equation representing the magnetization dynamics of an anisotropic nanoparticle subjected to a time-variant magnetic field. This equation presents interesting chaotic dynamics. In the parameter space, for some forcing frequency and magnetic strength of the applied field, one observes a transition from a regular periodic behavior to chaotic dynamics. The chaotic dynamics, close to the bifurcation, are characterized by type-III intermittency. Long epochs of quasi-regular dynamics followed by turbulent bursts. The characterization of the intermittencies has been done through four different techniques. The first method is associated with the computation of the Lyapunov exponents that characterize the chaotic regime. The second and third methods are associated with the statistics of the duration of the laminar epochs prior to a turbulent burst. The fourth method is associated with the subharmonic instability present in those laminar epochs and quantified through a Poincaré section method. At the end of the manuscript, we compare the result obtained by the different techniques and discuss the methods' limitations.

Keywords: Magnetization dynamics; chaos; type-III intermittency.

Submitted to: *Phys. Scr.*

1. Introduction

There are multiple routes to chaos [1–5]; perhaps the best-known mechanism is the period-doubling in which a cascade of bifurcations leads to chaotic states [4]. One notable route is the Ruelle-Takens-Newhouse scenario [6, 7], which essentially consists of an instability of a quasi-periodic state. Yet, another route appeared in the study of fluids and another physical systems, which is called *Intermittency* [1]. A seminal article by Manneville and Pomeau [8] described this new mechanism in the Lorenz system. They found these intermittencies when the reduced Rayleigh number is large, for values just above 166 [8, 9]. This chaotic route is characterized by an irregular alternation between long epochs of quasi-regular dynamics and turbulent bursts.

One distinguishes three types of transition to intermittency [10]. In all cases, we have a limit cycle (LC) that is stable before the transition and becomes unstable when a system's parameter is brought past the bifurcation threshold. The limit cycle's linear stability (Floquet theory) shows that the limit cycle can become unstable through three types of instability. The classification between intermittency of type I, II, and III relies on how the Floquet multiplier is crossing the unit disk in the complex plane. For intermittency of type I, the Floquet multiplier crosses the disk through +1. For type II, they are two complex conjugate multipliers that cross the unit disk through complex values. For intermittency of type III, the multiplier crosses the disk through -1. For intermittencies of type II and III, the bifurcation is always subcritical, which means that the weakly non-linear effects tend to increase the instability. Intermittency states were experimentally observed first in the Rayleigh-Benard convection [10] and later in several other dynamical systems [11–16]. Intermittencies have been observed in complex chemical reactions [17], electrochemical oscillators [19], quasi-periodically driven systems [18], or in thermoacoustic systems [20], to cite a few. Other studies on the subject can be found in Refs. [21–33].

The magnetization dynamics are inherently nonlinear, and complex states have been observed [34]. Indeed, several routes to chaos have been found for non-dissipative spin chains [35]. Studies of the chaos in magnetic systems using modern quantification techniques such as the Lyapunov exponents have been done in the context of the Landau-Lifshitz-Gilbert equation and its generalization. Those works can be found in Refs. [36–69]. Recently, theoretical-experimental research in nanomagnets in the monodomain regime have shown chaotic behaviors under the action of an electric current [70]. This study opens new venues to explore the complexity of magnetic nanostructures. From the theoretical point of view, two-dimensional phase diagrams of the largest Lyapunov exponent computed as a function of the system's parameters have been used to characterize the transitions between chaotic and regular states in magnetic nanoparticles [71]. The characterization of the route to chaos that occurs past the threshold has not yet been analyzed in depth.

The present work aims to examine a specific route to chaos for a parametrically driven anisotropic magnetic nanoparticle described by the Landau-Lifshitz-Gilbert (LLG) equation. In particular, we focus on the type-III intermittency dynamics that is observed in some region of the parameter space. The novelty lies in the fact that the magnetization has two limit cycles that are becoming unstable for the same bifurcation parameter due to a particular symmetry of the dynamical system that induces degeneracy. We found out that this issue does not substantially modify the type-III intermittency characteristics as long as we can distinguish between the two limit cycles. We characterize the regular to chaotic transition using several tools like the Lyapunov exponents, Poincare sections, and statistical distributions of the laminar epochs that exist prior to the turbulent bursts. The instability threshold is estimated with a very high degree of precision through four different methods. The manuscript is structured as follows: In Section 2, we describe the theoretical model. Section 3 is devoted to numerical results and discussions of the type-III intermittency. The summary of the different methods to characterize the bifurcation threshold is presented in Section 4. Finally, the conclusion and some future perspectives are outlined in Section 5.

2. Theoretical model

Let us suppose that a magnetic particle is represented by a magnetic monodomain [34, 70], such that its magnetization is depicted by a magnetization vector $\mathbf{M} = \mathbf{M}(t)$. The dimensionless LLG equation determines its evolution:

$$\kappa \frac{d\mathbf{m}}{d\tau} = -\mathbf{m} \times \mathbf{h}_{eff} - \alpha \mathbf{m} \times (\mathbf{m} \times \mathbf{h}_{eff}), \qquad (1)$$

where $\mathbf{m} = \mathbf{M}/M_s = (m_x, m_y, m_z)$ and $\tau = t|\gamma|M_s$. Here γ is the gyromagnetic factor, which is associated with the electron spin and its numerical value is $|\gamma| = |\gamma_e|\mu_0 \approx 2.21 \times 10^5 m A^{-1} s^{-1}$, M_s is the saturation magnetization and $\kappa = 1 + \alpha^2$, such that α is the dimensionless

dissipation coefficient. Typical orders of magnitude 10^{-2} or greater for cobalt, nickel or permalloy ($Ni_{80}Fe_{20}$) [34]. For cobalt materials, the experimental value of the saturation magnetization is, $M_{s[\mathrm{Co}]} \approx 1.42 \times 10^6\, A/m \approx 17.8\, kOe$, implying that time scale is $(|\gamma| M_{s[\mathrm{Co}]})^{-1} \approx 3ps$. In the case of magnetic materials with less saturation magnetization one can increase the time scale, like in the case of Nickel nanoparticles. Let us remark that this scaling of the variables leads to $|\mathbf{m}| = 1$, which is a conserved quantity of the dynamical system Eq. (1). This constraint can be used to monitor the accuracy of the numerical simulations.

The effective field, $\mathbf{h}_{eff}$, has a contribution from Zeeman and anisotropy energies. We consider that the external magnetic field has a harmonic time dependence as well as a constant term, such that they are perpendicular. Then, $\mathbf{h}_{eff}$ can be written as [71]:

$$\mathbf{h}_{eff} = \Big(h_x \sin(\Omega\tau) + \beta_x m_x\Big)\widehat{\mathbf{x}} + \Big(h_y \sin(\Omega\tau) + \beta_y m_y\Big)\widehat{\mathbf{y}} + \Big(h_z + \beta_z m_z\Big)\widehat{\mathbf{z}}, \tag{2}$$

where (h_x, h_y, h_z) are the dimensionless field amplitudes, Ω is the dimensionless frequency of the driven field, and the coefficients $(\beta_x, \beta_y, \beta_z)$ measure anisotropies. The dimensionless quantities are related with the physical ones by $\mathbf{h} = \mathbf{H}/M_s$ and $\Omega = \omega/(\gamma M_s)$. Standard values for the amplitude and frequencies are in the range of $10^0 - 10^1\ kOe$ and GHz, respectively [57, 66, 70]. On the other hand, the anisotropies consider the fact that the magnetic properties depend on the direction that is measured [72]. The anisotropies are due to several factors as, e.g., the crystalline, magneto-elastic, or the shape effects [34,72]. We point out that the magnetic anisotropy modifies the magnetic particles' dynamical behavior because it introduces intrinsic nonlinearities in the LLG equation [56, 64, 71]. Besides, let us remark that the system is non-autonomous because the external field is time-dependent.

2.1. Regular - Chaotic transitions

This nonlinear system has both dissipation and injection of energy, and therefore multiple behaviors are expected to appear. Indeed, recent works in the LLG equation regarding chaotic states can be found in Refs [36, 44, 48–50, 56]. One of the conventional methods to characterize the magnetization dynamics is through Lyapunov exponents [4, 73, 74], which quantify the divergence between infinitesimal closed trajectories. For a N-dimensional system, $d\mathbf{Y}/d\tau = \mathbf{F}(\mathbf{Y}, \tau)$, these exponents can be computed as

$$\lambda_i = \lim_{\tau\to\infty}\left[\frac{1}{\tau}\ln\left(\frac{|\delta Y_i(\tau)|}{|\delta Y_i(0)|}\right)\right], \tag{3}$$

where δY_i are solutions of the variational equation

$$\frac{\delta\mathbf{Y}}{d\tau} = \mathbf{J}\cdot\delta\mathbf{Y}, \tag{4}$$

such that $\mathrm{J}_{ab} = \partial F_a/\partial Y_b$. The exponents can be ordered in descending manner, $\lambda_1 > \lambda_2 > ... > \lambda_N$, with λ_1 being the largest Lyapunov exponent (LLE). If LLE is positive ($\lambda_1 > 0$) the state is chaotic, while if it is negative or zero ($\lambda_1 \leqslant 0$) the states are regular [4].

Let us remark that to ensure that the numerical solutions are accurately integrated, we use a modified fourth-order Runge-Kutta method that conserves the norm, $|\mathbf{m}| = 1$, with a fixed time step of $\Delta\tau = 0.01$. The Lyapunov spectrum is calculated by integrating the original dynamical system Eqs. (1) and three copies of the linearized dynamical equations to get the three Lyapunov exponents. The initial vectors for the linearized systems are ortho-normal, but they do not stay ortho-normal upon integration due to the chaotic dynamics. One must apply the Gram-Schmidt orthogonalization procedure periodically (here, we renormalize every $\tau = 1$ unit). The integration for determining the Lyapunov exponents has been continued for a time of $\tau = 2^{25}$. These very long simulations allow minimizing the error on the computed exponents. The typical standard error on the maximum Lyapunov exponent was approximately equal to 8.6×10^{-5}. The detail of the method for computing the Lyapunov spectrum can be found in the reference textbook by Gould & Tobochnik [76].

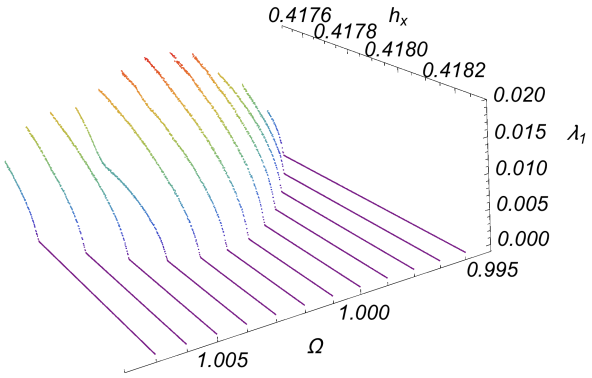

Figure 1: Largest Lyapunov exponent as a function of h_x for different values of Ω. The fixed parameters are: $h_y = 1$, $h_z = 3.52$, $\beta_x = 4$, $\beta_y = 0$, $\beta_z = -1$ and $\alpha = 0.05$.

In what follows, most of the parameters of Eqs. (1) will be fixed throughout the paper except for the parameters h_x and Ω. The rest of the parameters are fixed to: $h_y = 1$, $h_z = 3.52$, $\beta_x = 4$, $\beta_y = 0$, $\beta_z = -1$ and $\alpha = 0.05$. Figure 1 show the Largest Lyapunov exponent as a function of h_x for different values of Ω. We can observe that for all the values of Ω, the LLE becomes zero after a critical value of the h_x. Also, we observe that the LLE close to the transition decays almost linear, nevertheless far from the transition, its dependency becomes non-linear.

Figure 2 shows the behavior critical value of field in

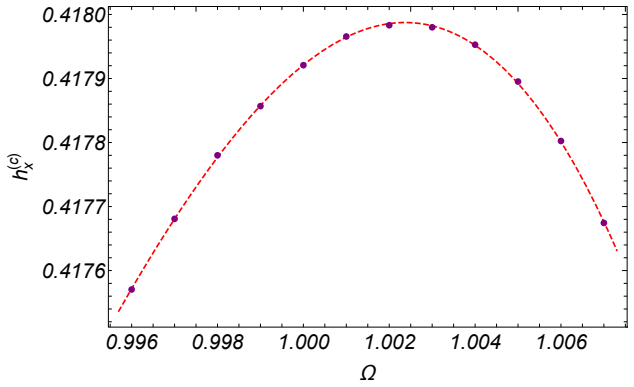

Figure 2: Critical value of field in which the Largest Lyapunov exponent becomes zero, $h_x^{(c)}$, as function of Ω. The rest of fixed parameters are the same of Fig. 1.

which the LLE becomes zero, $h_x^{(c)}$, respect to the frequency Ω. We can notice that $h_x^{(c)}$ has a polynomial dependence with Ω given by $h_x^{(c)} \approx -388.505\Omega^3 + 1155.56\Omega^2 - 1145.55\Omega + 378.911$. In the next section, we study the in detail the transition from periodic to chaotic behavior that occurs for $h_x \approx 0.418$ and $\Omega = 1$.

3. Evidences for type-III intermittency in the LLG equation

This section will illustrate through numerical integration of Eq. (1) the transition between periodic into a special type of chaotic behavior. In particular, we will show that the chaotic behavior observed is indeed of the type-III intermittency as explained in the Pomeau-Manneville theory [1]. When decreasing the main bifurcation parameter h_x below the threshold value $h_x^{(c)} \approx 0.418$ (threshold value will be determined accurately later) two limit cycles become unstable through a period-doubling instability, and one observes a chaotic behavior for $h_x < h_x^{(c)}$.

Let us remind the dynamical characteristics that are a positive sign of type-III intermittency: First, the positive Lyapunov exponent in the chaotic regime decays linearly towards zero when approaching the threshold value. Second, the unstable Floquet multiplier associated with the periodic solution crosses the unit disk through the real value -1 at the threshold value. Thirdly, the distribution of the laminar periods that are alternating between turbulence bursts follows a well-known statistical distribution with a characteristic exponential tail. The distribution tail size is directly related to the distance to the threshold in intermittencies of type-III. Fourthly, the second return map (in a Poincaré section) in the unstable regime displays a subharmonic mode growth. The second return map has a characteristic cubic functional form close to the instability threshold. The linear coefficient of the return map is directly proportional to the distance to the threshold value [21].

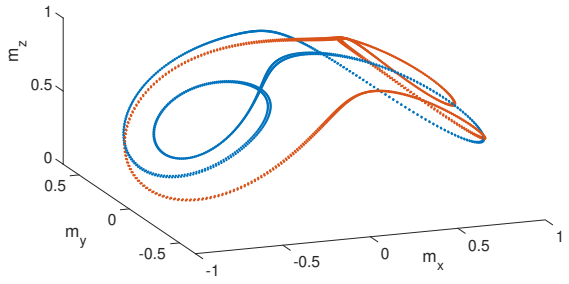

Figure 3: Phase space of the LLG equations. Coexistence of the two unstable periodic solutions for $h_x = 0.415$ and $\Omega = 1$. The rest of the parameters are the same of the Fig. 1.

Figure 3 illustrates the two coexisting limit cycles close to the bifurcation. In Fig. 3, the bifurcation parameter is set to $h_x = 0.415$, and the two limit cycles are slightly unstable. The coexistence of the two limit cycles is due to a degeneracy of the LLG equation Eq. (1). The symmetry relations to map one periodic solution to the other are as follows:

$$
\begin{aligned}
m_z &\longleftrightarrow m_z \\
m_y &\longleftrightarrow -m_y \\
m_x &\longleftrightarrow -m_x \\
\tau &\longleftrightarrow \tau + \pi/\Omega
\end{aligned}
$$

As it is known [1], the laminar periods (epoch periods) between turbulent bursts are longer as the dynamical system is brought closer to the bifurcation. We have performed very long simulations of over 24 million of the signal's basic period to get enough data to perform reliable statistics. In Fig. 4, we show an extract of a time series of the first component of the LLG equation m_x as a function of time. Here and throughout the paper, time is expressed in units of the basic period $T = 2\pi/\Omega$. Also shown in Fig. 4 is the definition of one laminar period (or epoch time) k_T between two consecutive turbulent bursts, which will also be measured in period unit time. Because the time series are very long, we have found that a better visualization of the signal is obtained when averaging the signal over a time period as indicated by the red curve $< m_x >$ in Fig. 4.

Contrary to the classical type-III intermittency, where a single limit cycle loses its stability through period-doubling. In the present case (due to the system's degeneracy), we have the coexistence of two limit cycles that are becoming unstable by period-doubling at the bifurcation threshold. It means that the relaminarisation phase during the turbulent burst can bring back the system

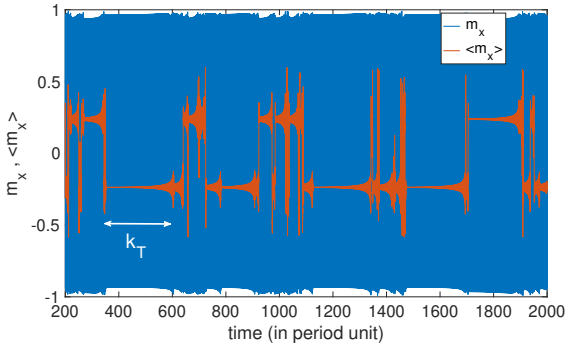

Figure 4: Time series of the component m_x (blue) and the moving average $< m_x >$ (in red). The average window width corresponds to one period T. The time scale is given in period unit time. The definition of an epoch time k_T is also illustrated. Here $h_x = 0.415$ and the rest of the parameters are same of Fig. 3.

close to any of the two limit cycles. This is well illustrated in Fig. 4, where after the turbulent burst, the system jumps either towards the other limit cycle or the former limit cycle.

At this stage, it becomes clear that the mere definition of the laminar periods has to be clarified. One approach uses the moving average signal and defines a transition when the moving average is crossing the zero line. Indeed, as shown in Fig. 4, the two unstable limit cycles have average values over a cycle comparable to ± 0.4. Each time that the moving average is crossing the zero line, we reset the laminar counter and start a new laminar epoch. A second approach, more refined, is to consider all the four possibilities for the transition as they actually happen in the system. This will be considered in more detail in section 3.2.

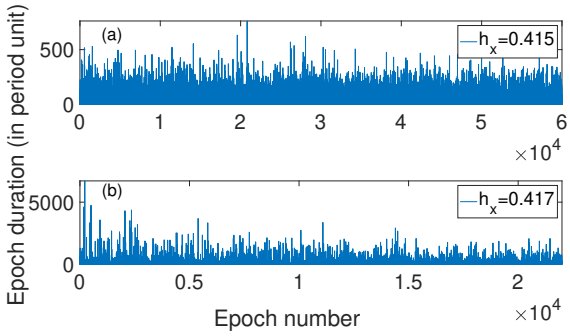

Figure 5: Successive epoch durations k_T as a function of the epoch numbers extracted from two very long time series (24 million of periods) as shown in Fig. 4. The upper panel (a) corresponds to a time series with $h_x = 0.415$ and the lower panel (b) corresponds to $h_x = 0.417$. Note that the vertical scale of the lower panel is one order of magnitude larger than for the upper panel.

3.1. Strong event transitions

In this subsection, we will first consider the more straightforward definition for the transition between different epochs as crossing the zero line of the average signal. This description is a simplification of the actual transitions that are occurring in the system (as shown in Fig. 4), but often, in an experimental setup, one does not have access to the full information of the dynamics and a precise definition of the laminar periods is not accessible. Therefore, this first method has interest on its own in the case of experiments where not all the information is readily available. We name these transitions "strong event transitions" because only when jumping from state Up to state Down (or vice-versa) will one count a transition. The self transitions Up-Up and Down-Down are not considered in this section but will be considered in Section 3.2.

Figure 5 shows an extract of successive laminar epochs that are registered for two different values of the parameter $h_x = 0.415$ (a) and $h_x = 0.417$(b). Note that the laminar periods shown in Fig. 4 are defined by the "strong event" definition. Now we are interested in testing if the Pomeau-Manneville theory [1] does apply in this case. Note that contrary to Pomeau-Manneville, here we have two unstable limit cycles, and in addition, we define the transition through the ad-hoc "strong event" definition. We know that as the system is brought closer to the bifurcation, the laminar epochs are getting larger. The statistical distribution of the laminar epoch has been derived by Pomeau-Manneville [1], and it follows:

$$P_{k_T} \sim \frac{e^{-2\epsilon k_T}}{(1-e^{-4\epsilon k_T})^{3/2}}, \tag{5}$$

where ϵ is the distance to the bifurcation threshold. Note that Eq. (5) contains a double asymptotic dependence. Indeed, we have:

$$\begin{aligned} P_{k_T} &\sim k_T^{-3/2} \quad \text{for} \quad \epsilon^{-1} \gg k_T \gg 1, \\ P_{k_T} &\sim e^{-2\epsilon k_T} \quad \text{for} \quad k_T \gg \epsilon^{-1}. \end{aligned} \tag{6}$$

In many instances, especially when dealing with experimental signals, it is often useful to ask how often a random variable is above a certain level. One defines the complementary cumulative distribution function (CCDF), which allows studying the tail of the distribution with greater accuracy. In the present case, we have:

$$\text{CCDF}(k_{T_0}) \sim \int_{k_{T_0}}^{+\infty} P_{k_T}\, dk_T \sim \frac{e^{-2\epsilon k_{T_0}}}{(1-e^{-4\epsilon k_{T_0}})^{1/2}}, \tag{7}$$

where $\text{CCDF}(k_{T_0})$ gives the distribution of the laminar epochs with a duration larger than a given value k_{T_0}. Again, as for Eq. (5) the CCDF has a double asymptotic dependence.

Figure 6 shows the non-normalized distribution of

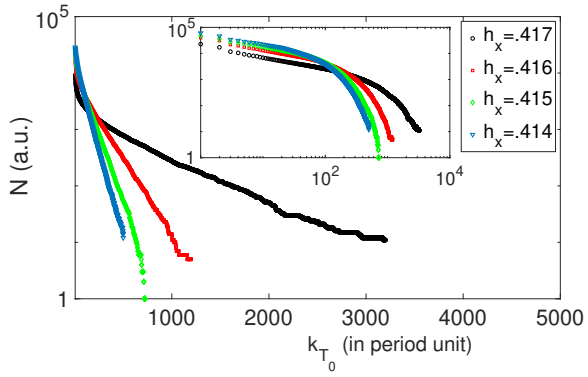

Figure 6: Statistics of laminar epochs exceeding a given duration of k_{T_0} (CCDF(k_{T_0})) not normalized. Symbol colors refer to the values of the bifurcation parameter. Black circles corresponds to $h_x = 0.417$; Red squares ($h_x = 0.416$); Green diamonds ($h_x = 0.415$); Blue triangles ($h_x = 0.414$). The main panel shows the exponential tail of the distributions for $k_{T_0} \gg \epsilon^{-1}$. The inset panel illustrates the power-law CCDF $\sim k_{T_0}^{-1/2}$ at low values of k_{T_0}.

laminar epochs that are longer than a given value k_{T_0}. the results were collected for simulations as long as 24 millions of the basic period. The distributions of CCDF shown in Fig 6 have two asymptotic behaviors. A power law $N \sim k_{T_0}^{-1/2}$ for intermediate values of k_{T_0} and an exponential tail for large value ($k_{T_0} \gg \epsilon^{-1}$) of the form $N \sim e^{-bk_{T_0}}$. We fitted the exponential tails for six consecutive values of the parameter h_x close to the bifurcation. The results of the fits are collected in Table 1, where the standard error (SE) is also given. Here we use the definition of the standard error as one standard deviation of the point estimate of parameter b.

Table 1: Tail parameter b of the exponential tails shown in Figure 6.

h_x	b	SE	R^2
0.413	1.965e-2	2.86e-5	0.9999
0.414	1.621e-2	1.49e-5	0.9999
0.415	1.276e-2	1.85e-5	0.9999
0.416	8.624e-3	7.82e-6	0.9999
0.417	4.322e-3	2.97e-6	0.9998
0.4178	5.819e-4	4.29e-7	0.9996

From Table 1, one observes that the exponential fit is in excellent agreement with the collected data (R^2 close to one) and that the parameter b is vanishing as we approach the bifurcation threshold. Indeed, from Eq. (7), the parameter b is directly proportional to the distance to the bifurcation.

One summarizes this section by acknowledging that even if one has only considered the "strong event" definition for a transition here and that one has two rather than one unstable limit cycle, the Pommeau-Manneville theory for the laminar period statistics is essentially correct. This is reminiscent of what happens in other statistical studies where the threshold for the definition of events does not affect the overall statistics essentially, as it happens, for example, in geophysical events (earthquakes, hurricanes,...) of different categories.

3.2. Detailed transitions

In the simulations of Eq. (1), one has access to all the state variables at any time. As illustrated in Fig. 4, after a laminar epoch, the system enters a turbulent regime and is then pushed towards one of the two unstable limit cycles. In general, one should therefore consider four types of transitions as summarized in the generic matrix below:

h_x		From state	
		Up	Down
To state	Up	N_{uu}	N_{du}
	Down	N_{ud}	N_{dd}

The number of transitions from a Up state to a Up state is given in the transition matrix by the number N_{uu}. The "strong event" transitions are indicated by N_{ud} and N_{du}. Because we need to cross the zero-line to add a "strong event" transition, the above transition matrix is symmetric (or at least the numbers N_{ud} and N_{du} should not differ by more than one unit). The numbers in the transition matrix will depend on the parameter h_x. The numbers of transitions are calculated for six different values of the parameter h_x and are given in Appendix A.

Before discussing the results of the transition matrices, let us explain in detail the detection algorithm that we have used for deciding if the system is in one of the three following states: laminar regime "up"; laminar regime "down"; or relaminarisation regime (also called "burst"). The algorithm analyzes the x component of the magnetization vector $\mathbf{m}$ period after period, as shown in Fig 7. For each basic period, we search for two representative points of the signal: the highest local minimum (indicated by black asterisks in Fig 7); and the second-highest local maxima denoted in Fig 7 by red squares. It becomes apparent from Fig 7 that the lowest laminar state ("down" state) is characterized by growing alternating (subharmonic) fluctuations of the second local maxima around the value of $m_x \approx -0.4041$ and also weaker fluctuations of the highest local minimum around the value $m_x \approx -0.8898$. Due to symmetry, the "up" state regime is characterized by growing fluctuations of the highest minimum around the value of $m_x \approx 0.4041$ and also weaker fluctuations of the second local maximum around the value $m_x \approx 0.8898$. Our detection algorithm is based on those characteristics to decide if the system is

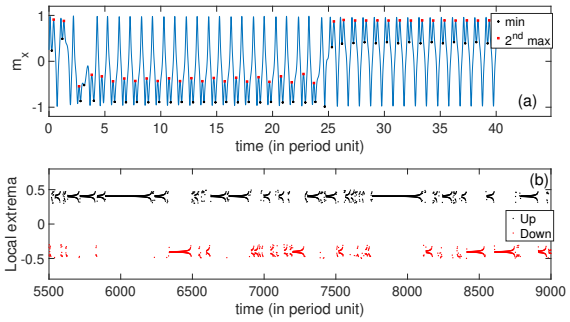

Figure 7: a) Representative points taken during each period from the x component of the magnetization vector $\mathbf{m}$. The black asterisks indicate the highest local minimum attained during the corresponding analyzed period. The red squares indicate the second-highest local maxima attained during the corresponding period. b) Stroboscopic representative values (Poincaré sections) taken after each period for the two unstable periodic orbits. The red dots correspond to the iterations close to the lower solution. The black dots correspond to the iterations close to the upper solution. The parameter is fixed to $h_x = 0.415$.

in one of the three aforementioned states ("Up"; "Down"; or "burst"). Figure 7b illustrates the results of the detection algorithm over a period of 3,500 periods.

This refined algorithm allows filling the transition matrix with all the collected transitions. While this algorithm is simple, it is not always practical as we do not always have access to the full information of the dynamical system.

Thanks to this algorithm, we are now able to test if the symmetry between states up and down is maintained. Indeed, in principle, due to the degeneracy of the system, both unstable limit cycles should have the same behavior close to the bifurcation threshold. We perform a χ^2 test from the transitions matrices (see Appendix A) to determine if the symmetry up-down is conserved.

In Table 2, we denote by $\hat{p}_{uu}$ and $\hat{p}_{dd}$ the estimated transition probabilities from the measured transition matrix tables (using maximum likelihood estimates). If symmetry were perfectly satisfied, the "self" transition probabilities should be equal and $p_{uu} = p_{dd} = p_{\text{self}}$, again estimated by the following expression:

$$\hat{p}_{\text{self}} = \frac{\hat{p}_{uu} + \hat{p}_{dd}}{2} \tag{8}$$

Table 2: Transition matrix results with χ^2 tests to determine if the symmetry up-down is conserved. N corresponds to the total number of transitions.

h_x	N	$\hat{p}_{uu}$	$\hat{p}_{dd}$	$\hat{p}_{\text{self}}$	χ^2_2	p-value
0.413	743262	0.2516	0.2524	0.2520	0.965	0.617
0.414	633074	0.2701	0.2715	0.2708	2.26	0.323
0.415	562637	0.2723	0.2733	0.2728	0.904	0.636
0.416	351450	0.2426	0.2431	0.2428	0.218	0.897
0.417	303387	0.2511	0.2493	0.2502	2.04	0.360
0.4178	116851	0.2619	0.2603	0.2611	0.557	0.757

Table 2 shows that there is no statistically significant difference between the number of transition "Up-up" and "Down-down." The probabilities $\hat{p}_{uu}$ and $\hat{p}_{dd}$ are not statistically different, as indicated by the p-value of the last column of Table 2. Furthermore, Table 2 shows that $\hat{p}_{\text{self}} \approx 0.25$ meaning that there is approximately the same number of transitions for "strong events" as for "self" transitions. This was not expected, and it is presumably something special about this specific dynamical system.

Figure 8 shows the transient proportions of the different transition types in the system when the dynamics evolve. As we have mentioned in the Introduction, we have simulated very long time series, and Fig. 8 shows that the time scale to reach steady values is indeed very long when we are close to the bifurcation threshold. Note that the "strong events," related to the probabilities p_{ud} and p_{du}, settle more quickly than the "self" transitions p_{uu} and p_{dd}. Also, quite unexpectedly, in Fig. 8, one observes that the four probabilities converge to the same value of approximately one quarter.

3.3. Epoch duration statistics

In this section, we provide the statistics associated with the epoch durations prior to a transition. We show in Fig. 9 that we are now considering all types of transitions that may occur in the system. Note that when we consider the detailed transitions, the epoch duration is smaller than when we consider the "strong events" type of transitions. In Fig. 9 τ_{all} is obtained by collecting the four different types of detailed transitions, i.e., τ_{uu}; τ_{dd}; τ_{ud}; τ_{du}. From Fig. 9, it becomes apparent that we also have an exponential tail for the statistical distributions when considering the detailed transitions. However, the value of the exponential decay is somewhat larger (in absolute value), i.e., the distribution tail is smaller for τ_{all} than in the case of the "strong events" type of transitions (compare with τ_{se} in Fig. 9). As we have done in the case of the "strong events" type of transitions, we perform a fit for the distribution tail of the CCDF of τ_{all}, and the results are collected in Table 3. Note that we use here the notation $N \sim e^{-\tilde{b}k_{T_0}}$ for the decaying tail in order to distinguish from the fit of the "strong events" tails.

The results collected in Table 3 show that as it happened in the case of the fitting of the "strong events"

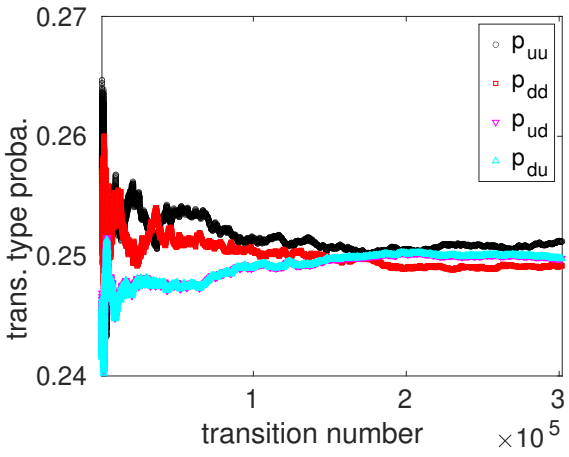

Figure 8: Evolution of the transient proportions of the different transition types. Here, the total number of transitions between laminar epochs is 303,387. The total simulation time is 24,371,366 basic periods. Black circles refer to the proportion of transitions "Up-Up." Red squares refer to the proportion of transitions "Down-Down." Magenta triangles pointing downwards indicate the proportion of transitions "Up-Down." Cyan triangles pointing upwards indicate the proportion of transitions "Down-Up." The figure is drawn with the bifurcation parameter set to $h_x = 0.417$.

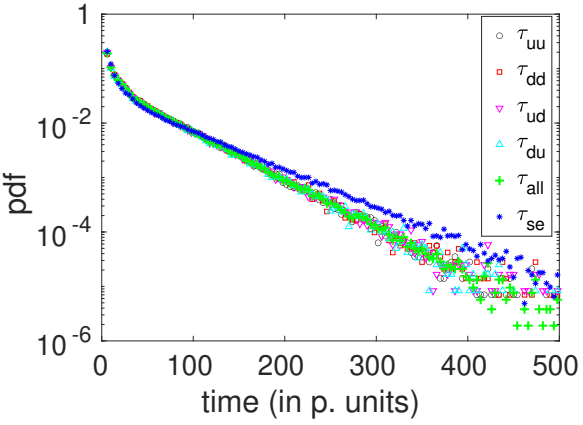

Figure 9: PDFs of the laminar epoch distributions prior to a given transition event. Black circles refer to τ_{uu}, i.e., the time distribution of laminar epochs preceding an Up-Up transition (see text for details). Plus sign symbols in green refer to τ_{all} the aggregate of the four individual distributions τ_{uu}; τ_{dd}; τ_{ud}; τ_{du}. The asterisk symbols τ_{se} refer to the time distribution preceding a "strong" event (see text for definition). All the distributions exhibit an exponential tail. The fits of the tails are for the corresponding CCDF distributions and are given in Table 3. The figure is drawn with parameter set to $h_x = 0.414$.

tails, the coefficient of the exponential fit $\tilde{b}$ vanishes as it approaches the bifurcation threshold. This will allow getting a new independent estimate of the bifurcation threshold from this new series of exponential fits.

Table 3: Tail parameter $\tilde{b}$ of the exponential tails of the CCDF of the corresponding PDF distribution τ_{all} shown in Fig 9.

h_x	$\tilde{b}$	SE	R^2
0.413	2.491e-2	6.15e-5	0.9999
0.414	1.990e-2	4.10e-5	0.9999
0.415	1.501e-2	1.97e-5	0.9999
0.416	9.842e-3	1.03e-5	0.9999
0.417	4.773e-3	3.77e-6	0.9999
0.4178	5.957e-4	4.17e-7	0.9996

3.4. Permanency phase statistics

In this section we also provide the statistics related to the total permanence time in the three states "Up", "Down", and "burst." This is somewhat different from the transition-type statistics that we have studied in Section 3.2. Here, we are interested in checking if the dynamical system spends the same amount of time in the "Up" and "Down" states as it should be due to the symmetry of the two limit cycles. Figure 10 shows that after some transient, the system equilibrates towards a quasi-steady state where the amount of time spent in the "Up" and "Down" states is nearly the same. Recall that the total duration of the simulations is over 24 million of the basic period. In Appendix A, Table A1 collects the amount of time in the different phases as well as the percentiles of the distribution of the laminar phases. A simple χ^2 square test shows that the time spend in the "Up" and "Down" is not statistically equivalent. Here a word of caution is in order. In the hypothesis testing, we assume that the basic period is the correct unit time scale to consider a transition between the two states. This is certainly not quite correct, and a better time scale would be the inverse of the parameter b from Table 1, which is a more physical time scale associated with the intermittency phenomenon. In addition, in the Table A1 are the percentiles P_{50}, P_{90}, P_{95} of the laminar periods given. Here, we have collected on one hand the laminar periods corresponding to all the transitions, and on the other hand, the "strong event" transitions. Table A1 shows that the higher percentiles for the "strong event" transitions are considerably larger than the corresponding ones for the "all" transition events.

3.5. Poincaré sections

As observed from Fig. 4, the instability prior to a "burst" or relaminarisation epoch takes place through a subharmonic

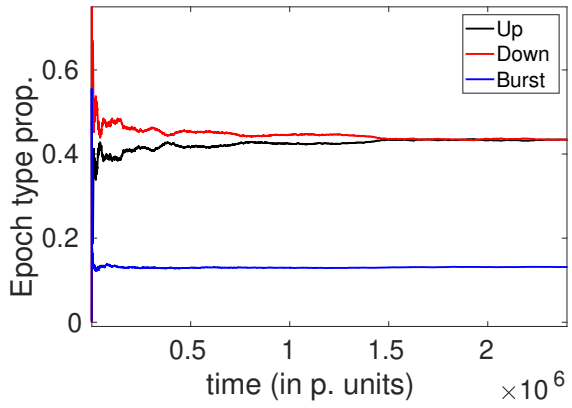

Figure 10: Transient proportions of the different epoch types (Up, Down and Burst states). The total simulation time corresponds to 24,371,366 basic periods. Here we have plotted the transient up to 2.4 million of the basic period. The black line refers to the transient proportion of time spent in the Up epochs. The red line refers to the transient proportion of time spent in the Down epochs. The blue line refers to the transient proportion of burst epochs. The figure is drawn with parameter $h_x = 0.417$.

instability. This is indeed the hallmark of type-III intermittencies, and this can be put forward in a Poincaré section study. This section is devoted to the study of the Poincaré sections extracted from the long simulations of the chaotic dynamics Eqs. (1).

The onset of intermittencies corresponds to the instability of one of the two limit cycles (LC) that are slightly unstable. The hallmarks defined in Section 3.2, i.e., the highest local minimum and the second-highest maximum, will serve as the definition for two Poincaré sections. One of the sections will follow the stability of one of the LC, and the other section will correspond to the other unstable LC. Close to the unstable LC, one can write a mathematical expansion in terms of the amplitude. These amplitudes are perturbations of the unstable LC. These perturbations can be described at lower order as follows:

$$I_{n+1} = -(1+\epsilon)I_n + AI_n^2 + BI_n^3 + \mathcal{O}(I_n^3). \qquad (9)$$

where A and B are numerical constants; ϵ is the distance to the threshold, and the I_n indicates the strength of the perturbation at iteration n in the Poincaré map. When considering a subharmonic instability, it is easier to deal with the second return map (i.e., the application of the application Eq. (9)). If ϵ is small, we get at first order in ϵ:

$$I_{n+2} = (1+2\epsilon)I_n + cI_n^3 \qquad (10)$$

where $c = -2A^2 - 2B$. Note that the quadratic term is vanishing as it is multiplied by the infinitesimal ϵ, which is typical of type-III intermittency. In addition, in Eq. (10), we are left with a slightly greater than one linear term that indicates the instability rate. Actually, this is directly connected with the Floquet multiplier of the instability. In the present case, the cubic term c is positive, and the instability is not bounded by weakly nonlinear terms. Rather the unstable trajectory is performing a large excursion in the phase space, and after a relaminarisation period, it is re-injected close to one of the two unstable LCs.

Using Eq. (10) for our data at different values of the bifurcation parameter h_x will lead to another way to determine the bifurcation threshold. For parameter h_x in the range between $[0.413-0.4178]$, we have examined the long simulations (up to over 24 million of the basic period), and we keep the longest laminar epochs (independently of the type of transition that ends the laminar epoch). We analyze approximately the 1,500 longer laminar epochs for each value of the bifurcation parameter h_x. We fit the second return map according to Eq. (10), where we allow only for a linear and cubic term as fitting parameters. In general, the goodness of fit is excellent, with an R^2 very close to one. Because we have kept over 1,500 epochs, we get a good sampling distribution for the linear parameter and we report the mean value and standard deviation of the linear term of Eq. (10) from this sampling distribution. Actually, we report the linear term as $1+a\epsilon$ because the projection of the Poincaré section does not ensure to have exactly a linear term of the form $1+\epsilon$ but rather a correction term which is linearly proportional to ϵ as in the term $1+a\epsilon$.

Table 4 reports the mean values of the linear fitting parameters as well as their standard deviations for several h_x. This shows, as expected, that the linear term is vanishing when approaching the bifurcation threshold. The cubic term of the fit from Eq. (10) is also given in Table 4 for completeness.

Table 4: Linear and cubic fitting parameters from Eq. (10). The standard error is equal to a standard deviation of the corresponding sampling distribution.

h_x	$a\epsilon$	$SE_{a\epsilon}$	c	SE_c
0.413	4.781e-2	1.04e-3	109.1	4.19
0.414	3.829e-2	1.02e-3	108.6	4.69
0.415	2.866e-2	8.33e-4	108.0	5.37
0.416	1.893e-2	6.41e-4	106.6	5.94
0.417	9.139e-3	4.24e-4	102.6	6.74
0.4178	1.14e-3	5.90e-5	95.8	3.52

4. Approximation of the bifurcation threshold

The determination of the bifurcation threshold of any dynamical system is almost always tricky. Especially when dealing with noisy experimental data, one often has trouble determining with accuracy the bifurcation threshold. This

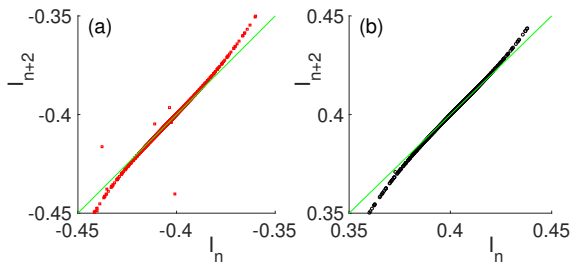

Figure 11: Second return maps (Poincaré maps) for the two unstable periodic orbits. The red squares in panel (a) refer to successive iterations of the lower solution. The black circles in panel (b) refer to successive iterations of the upper solution, as shown in Fig 6. The parameter is fixed to $h_x = 0.415$.

manuscript shows that one has different techniques that can help to determine the bifurcation threshold quite accurately.

Table 5: Comparison of the different estimates for the bifurcation threshold $h_x^{(c)}$. The confidence intervals (CI) are obtained through a bootstrap method [75].

Method	$h_x^{(c)}$	95% CI
Poincaré	0.417932	[0.417870 – 0.417997]
"Strong events"	0.418077	[0.418073 – 0.418080]
"All events"	0.417938	[0.417933 – 0.417943]
Lyapunov	0.417920	[0.417919 – 0.417921]

In Table 5, we have compared the different estimates of the bifurcation threshold $h_x^{(c)}$. In addition to a point estimate for the bifurcation threshold $h_x^{(c)}$, Table 5 also provides a 95 % confidence interval (CI) for each of the estimates. These CI were obtained through a simple bootstrap method. Basically, we use 50,000 repetitions of the linear fits for the different methods. This provides a sampling estimation, and we use the percentiles 2.5 and 97.5 as a measure of the distribution spread [75].

5. Conclusions

The present manuscript aims to propose several alternatives to characterize the bifurcation threshold in a transition to type-III intermittencies. We have shown through four different techniques that the values obtained for the bifurcation threshold are consistent. The best method, the one associated with the Lyapunov exponents' computation, is also the less practical. Indeed, from experimental data, it is more complicated to extract accurately the Lyapunov exponents associated with the dynamics [77].

An important outcome from our analysis is that if we capture long enough signals, we can reach a very high accuracy, even with experimental signals for determining the bifurcation thresholds.

One clear limitation of the present work is associated with the accuracy of the data. Indeed, we need to either determine in which phase the system is (laminar or burst phase), or in the case of the Poincaré section technique, be able to follow the subharmonic instability. This is somewhat the main limitation of the methods, and in the case of experimental setups, one may need to do some filtering to clean the noisy data.

In the case of the physical system that we have studied, i.e., the parametrically driven dissipative magnetization dynamics of an anisotropic nanoparticle, one has found that the intermittency region is relatively narrow in the parameter space. This is in contrast with what happens in other systems like in fluid convection [21], where the intermittency dynamics exist for a broader range of parameters.

Many dynamical systems exhibit type-III intermittency, and we have provided some tools for further studying their characteristics near the threshold. Future direction to this research would connect two or more of these dynamical systems and see how it affects the bifurcation thresholds and the intermittency dynamics.

Acknowledgments

JB acknowledges financial support from the Spanish project with reference: SAF-2017-88019-C3-2-R. LMP and DL acknowledge partial financial support from FONDECYT 1180905. DL acknowledges partial financial support from Centers of excellence with BASAL/ANID financing, AFB180001, CEDENNA.

References

[1] Bergé P, Pomeau Y and Vidal Ch 1987 *Order within chaos: Towards a deterministic approach to turbulence*. (New York: John Wiley & Sons)
[2] Eckmann J P 1981 *Rev. Mod. Phys.* **53**, 643.
[3] Ott E 2002 *Chaos in Dynamical Systems, second edition*. (Cambridge: Cambridge University Press)
[4] Sprott J C 2003 *Chaos and Time-Series Analysis*. (Oxford: Oxford University Press)
[5] Grebogi C, Ott E and Yorke J A 1983 *Physica D* **7**, 181.
[6] Ruelle D and F Takens 1971 *Commun. Math. Phys.* **20**, 16.
[7] Newhouse S, Ruelle D, and Takens F 1978 *Commun. Math. Phys.* **64**, 35.
[8] Manneville P and Pomeau Y 1979 *Physics Letters* **75A**, 1.
[9] Pomeau Y and Manneville P 1980 *Commun. Math. Phys.* **77**, 189.
[10] Bergé P, Dubois M, Manneville P and Pomeau Y 1980 *J. Phys.* **41**, L341.
[11] Jeffries C and Perez J 1982 *Phys. Rev. A* **26**, 2117.
[12] Dubois B, Rubio M A and Bergé P 1983 *Phys. Rev. Lett.* **51**, 1446.
[13] Huang J Y and Kim J J 1987 *Phys. Rev. A* **34**, 1495.
[14] Aubty N, Holmes P, Lumley J L and Stone E 1988 *J. Fluid Mech.* **192**, 115.
[15] Baier G, Wegmann K and Hudson J L 1989 *Phys. Lett. A* **141**, 340.
[16] Price T J and Mullin T 1991 *Physica D* **48**, 29-52.

[17] Possio C T and Pellegrini L 1994 *Chemical Engineering Science* **49**, 131.
[18] Prasad A, Mehra V and Ramaswamy R 1997 *Phys. Rev. Lett.* **79**, 21.
[19] Kiss I Z and Hudson J L 2001 *Physical Review E* **64**, 046215.
[20] Guan Y, Gupta V and Li L K 2020 *J. Fluid Mech.* **894**, R3.
[21] Dubois M, Rubio M A and Berge P 1983 *Phys. Rev. Lett.* **51**, 1446.
[22] Antoranz J C and Mori H 1985 *Physica D* **16**, 184-202.
[23] Honda K, Kodama H and Sato S 1990 *Physics Letters A* **149**, 2.
[24] Kreisberg N, McCormick W D and Swinney H L 1991 *Physica D* **50**, 463-477.
[25] Tambe S S and Kulkarni B D 1993 *Chemical Engineering Science* **48**, 2817-2821.
[26] Heagy J F, Platt N and Hammel S M 1994 *Physica Review E* **49**, 2.
[27] Malasoma J M, Werny P and Boiron M A 2003 *Chaos, Solitons and Fractals* **15**, 487-500.
[28] Alvarez-Llamoza O, Cosenza M G and Ponce G A 2008 *Chaos, Solitons and Fractals* **36**, 150-156.
[29] Miliou A N, Stavrinides S G, Valaristos A P and Anagnostopoulos A N 2009 *Nonlinear Analysis* **71**, e3-e20.
[30] Cosenza M G, Alvarez-Llamoza O and Ponce G A 2010 *Commun Nonlinear Sci Numer Simulat* **15**, 2431-2435.
[31] Elaskar S, del Rio E and Donoso J M 2011 *Physica A* **390**, 2759-2768.
[32] Medeiros E S, Caldas I L, Murilo S. Baptista M S and Feudel U 2017 *Scientific Reports* **7**, 42351.
[33] Vassilicos J C 2011 *Intermittency in turbulent flows*. (Cambridge: Cambridge U. Press).
[34] Bertotti G, Mayergoyz I, and Serpico C 2009 *Nonlinear magnetization dynamics in nanosystems*. (Amsterdam: Elsevier)
[35] Jaroszewicz A, and Sukiennicki A 1992 *J. Magn. Magn. Mater.* 104-107 867-868.
[36] Alvarez L F, Pla O and Chubykalo O 2000 *Phys. Rev. B.* **61**, 11613.
[37] Bertotti G, Serpico C and Mayergoyz I D 2001 *Phys. Rev. Lett.* **86**, 724.
[38] He P B and Liu W M 2005 *Phys. Rev. B* **72**, 064410.
[39] Laroze D and Vargas P 2006 *Phys. B* **372**, 332.
[40] Sementsov D I and Shutyi A M 2007 *Phys. Usp.* **50**, 793.
[41] Horley P P, Vieira V R, Gorley P M, Dugaev V K and Barnas J 2008 *Phys. Rev. B.* **77**, 054427.
[42] Laroze D and Perez L M 2008 *Physica B.* **403**, 473.
[43] Laroze D, Vargas P, Cortes C and Gutierrez G. 2008 *J. Magn. Magn. Mater.* **320**, 1440.
[44] Shutyi A M and Sementsov D I 2009 *Chaos* **19**, 013110.
[45] Shutyi A M and Sementsov D I 2009 *Crystallogr. Rep.* **54**, 98.
[46] Vagin D V and Polyakov P 2009 *J. App. Phys.* **105**, 033914.
[47] Khivintsev Y, Kuanr B, Fal T J, Haftel M, Camley R E, Celinski Z and Mills D L 2010 *Phys. Rev. B.* **81**, 054436.
[48] Smith R K, Grabowski M and Camley R E 2010 *J. Magn. Magn. Mater.* **322**, 2127.
[49] Laroze D, Bragard J, Suarez O J and Pleiner H 2011 *IEEE Trans. Magn.* **47**, 3032.
[50] Bragard J, Pleiner H, Suarez O J, Vargas P, Gallas J A C and Laroze D 2011 *Phys. Rev. E.* **84**, 037202.
[51] Khivintsev Y, Marsh J, Zagorodnii V, Harward I, Lovejoy J, Krivosik P, Camley R E and Celinski Z 2011 *Appl. Phys Lett.* **98**, 042505.
[52] Laroze D, Becerra-Alonso D, Gallas J A C and Pleiner H 2012 *IEEE Transations on Magnetics* **48**, 3567-3570.
[53] Urzagasti D, Laroze D, Clerc M G and Pleiner H 2013 *EPL* **104**, 40001.
[54] Pérez L M, Suarez O J, Laroze D and Mancini H L 2013 *Cent. Eur. J. Phys.* **11**, 1629-1637.
[55] Denisov S I, Lyutyy T V, Pedchenko B O and Babych H V 2014 *J. Appl. Phys.* **116**, 043911.
[56] Pérez L M, Bragard J, Mancini H L, Gallas J A C, Cabanas A M, Suarez O J and Laroze D 2015 *Net. and Het. Med.* **10**, 209.
[57] Phelps M G, Livesey K L, Ferona A M and Camley R E 2015 *EPL* **109**, 37007.
[58] Lyutyy T V, Denisov S I, Peletskyi A Y and Binns C 2015 *Phys. Rev. B.* **91**, 054425.
[59] Urzagasti D, Becerra-Alonso D, Perez L M, Mancini H L and Laroze D 2015 *J Low Temp Phys.* **181**, 211-222.
[60] Horley P P, Kushnir M Y, Morales-Meza M, Sukhov A and Rusyn V 2016 *Physica B.* **486**, 60-63.
[61] Pivano A and Dolocan V O 2016 *Phys. Rev. B.* **93**, 144410.
[62] Denisov S I, Lyutyy T V, Pedchenko B O and Hryshko O M 2016 *Phys. Rev. B.* **94**, 024406.
[63] Suarez O J, Laroze D, Martinez-Mardones J, Altbir D and Chubykalo-Fesenko O 2017 *Phys. Rev. B.* **95**, 014404.
[64] Ferona A M and Camley R E 2017 *Phys. Rev. B.* **95**, 104421.
[65] Cabanas A M, Pérez L M and Laroze D 2018 *J. Magn. Magn. Mater.* **460**, 320-326.
[66] Okano G and Nozaki Y 2018 *Phys. Rev. B.* **97**, 014435.
[67] Ferona A M and Camley R E 2019 *Phys. Rev. B.* **99**, 064405.
[68] Velez J A, Mosso E and Suarez O J 2019 *Journal of Magnetics* **24**, 402-407.
[69] Gibson C, Bildstein S, Hartman J A L and Grabowski M 2020 *J. Magn. Magn. Mater.* **501**, 166352.
[70] Montoya E, Perna S, Chen Y, Katine J A, d'Aquino M, Serpico C and Krivorotov I N 2019 *Nat. Commun.* **10**, 543.
[71] Vélez J A, Bragard J, Pérez L M, Cabanas A M, Suarez O J, Laroze D and Mancini H L 2020 *Chaos* **30**, 093112.
[72] Cullity B D and Graham C D 2009 *Introduction to Magnetic Materials, 2nd edition*. (New Jersey: J. Wiley IEEE Press)
[73] Wolf A, Swift J B, Swinney H L and Vastano J A 1985 *Physica D* **16**, 285.
[74] Pikovsky A and Politi A 2016 *Lyapunov Exponents: A Tool to Explore Complex Dynamics*. (Cambridge U. Press)
[75] Rice J A 1995 *Mathematical statistics and data analysis, 2nd Ed.* (Berkeley: University of California)
[76] Gould H and Tobochnik J 1988 *An introduction to computer simulation methods : applications to physical systems*. (Massachusetts: Addison-Wesley)
[77] Kantz H and Schreiber T 2004 *Nonlinear Time Series Analysis*. (Cambridge: Cambridge University Press)

Appendix A. Statistics of the number of transitions between the two states

In this Appendix, we have gathered the results of the number of transitions as characterized in Section 3.2. The absolute number of transitions is decreasing as we approach the bifurcation threshold. This is a consequence of the fact that the we have larger laminar epochs between the different transitions. Note that the laminar epochs of duration less than two periods have been removed from the statistics.

$h_x = 0.413$

To state \ From state	Up	Down
Up	186972	184362
Down	184362	187566

$h_x = 0.414$

To state \ From state	Up	Down
Up	171013	145084
Down	145085	171892

$h_x = 0.415$

To state \ From state	Up	Down
Up	153234	127822
Down	127821	153760

$h_x = 0.416$

To state \ From state	Up	Down
Up	85261	90367
Down	90368	85454

$h_x = 0.417$

To state \ From state	Up	Down
Up	76177	75795
Down	75795	75620

$h_x = 0.4178$

To state \ From state	Up	Down
Up	30598	27919
Down	27920	30414

Table A1: Summary of the total epoch durations and percentiles of the epoch durations prior to a transition as a function of the bifurcation parameter h_x. Note that the epoch duration are given in term of the basic period. The χ^2 square test check for the null hypothesis that the Up and Down durations are equal. For the computation of the percentiles of the epoch duration prior to a burst we have pruned the distributions from all the epochs with a duration less than three basic periods. Note that the total time amounts to 24,371,366 basic periods. We have reported the percentiles 50 to 99 because we are interested in the right tail of the epoch distribution (which is known to follow an exponential distribution).

	Epoch durations					All events				Only "strong events"			
h_x	Up	Down	Burst	χ^2	p-val.	P_{50}	P_{90}	P_{95}	P_{99}	P_{50}	P_{90}	P_{95}	P_{99}
0.413	8872849	8878208	6620308	1.62	0.203	16	74	102	166	15	87	123	206
0.414	9315018	9361258	5695090	114	< 1.e-16	18	91	126	206	16	105	147	248
0.415	9566694	9618248	5186424	138	< 1.e-16	19	109	154	261	14	116	171	299
0.416	10610502	10575775	3185089	56.9	4.5.e-14	27	196	267	429	19	206	288	474
0.417	10662128	10552688	3156550	564	< 1.e-16	25	229	353	687	15	212	338	710
0.4178	11576493	11493539	1301334	298	< 1.e-16	26	533	1278	3858	14	327	910	3451